Efficient axonal transport of endolysosomes relies on the balanced ratio of microtubule tyrosination and detyrosination

Anja Konietzny, Yuhao Han, Yannes Popp, Bas van Bommel, Aditi Sharma, Philippe Delagrange, Nicolas Arbez, Marie-Jo Moutin, Leticia Peris, Marina Mikhaylova

Efficient axonal transport of endolysosomes relies on the balanced ratio of microtubule tyrosination and detyrosination

Running title: The tubulin code defines endolysosomal axonal transport

Anja Konietzny[1,2,3]*, Yuhao Han[1,2,5,6], Yannes Popp[1,2,7], Bas van Bommel[2,8], Aditi Sharma[4], Philippe Delagrange[9], Nicolas Arbez[9], Marie-Jo Moutin[4γ], Leticia Peris[4γ], Marina Mikhaylova[1,2*]

[1] RG Optobiology, Institute of Biology, Humboldt Universität zu Berlin, Berlin, Germany
[2] Guest Group "Neuronal Protein Transport", Center for Molecular Neurobiology, ZMNH, University Medical Center Hamburg-Eppendorf, Hamburg, Germany, discontinued in August 2023
[3] Institute of Industrial Science, The University of Tokyo, Tokyo, Japan
[4] Univ. Grenoble Alpes, Inserm U1216, CNRS, Grenoble Institut Neurosciences, 38000 Grenoble, France
[5] Centre for Structural Systems Biology, Hamburg, 22607 Germany
[6] Structural Cell Biology of Viruses, Leibniz Institute of Virology (LIV), Hamburg, 20251 Germany
[7] Charité – Universitätsmedizin Berlin, Einstein Center for Neurosciences Berlin, 10117, Berlin, Germany
[8] Institute for Chemistry and Biochemistry, Freie Universität Berlin, Berlin, Germany
[9] Institut de Recherche Servier, Croissy, France
[γ] *equal contribution*
* Correspondence: anja-k@iis.u-tokyo.ac.jp and marina.mikhaylova@hu-berlin.de

Keywords: microtubule post-translational modification, axonal trafficking, axon initial segment, tubulin-tyrosine ligase, vasohibins

Summary Statement

Despite opposite effects on microtubule dynamics, shifting the balance of microtubule tyrosination/detyrosination in either direction resulted in surprisingly similar defects in axonal organelle transport.

Abstract

In neurons, the microtubule (MT) cytoskeleton forms the basis for long-distance protein transport from the cell body into and out of dendrites and axons. To maintain neuronal polarity, the axon initial segment (AIS) serves as a physical barrier, separating the axon from the somatodendritic compartment and acting as a filter for axonal cargo. Selective trafficking is further instructed by axonal enrichment of MT post-translational modifications, which affect MT dynamics and the activity of motor proteins. Here, we compared two knockout mouse lines lacking the respective enzymes for MT tyrosination and detyrosination and found that both knockouts led to a shortening of the AIS. Neurons from both lines also showed an increased immobile fraction of endolysosomes present in the axon, whereas mobile organelles displayed shortened run distances in the retrograde direction. Overall, our results highlight the importance of maintaining the balance of tyrosinated/detyrosinated MT for proper AIS length and axonal transport processes.

Introduction

The complex, polarized morphology of neurons with their extensively branched neurites presents various challenges for the maintenance of cellular homeostasis. Neurons contain an elaborate intracellular recycling system within the soma, dendrites and axon that balances the transport of newly synthesized cellular components with the removal of aged and damaged ones. At the same time, transport processes need to be highly selective to maintain the molecular identities of the somatodendritic and the axonal compartments. The master regulator of polarized trafficking is a complex structure spanning the first 20-60 µm of the axon, called the axon initial segment (AIS), which selectively restricts cargo transport and is essential for the generation of action potentials (Nakada et al., 2003; Petersen et al., 2014). The AIS is composed of various elements, including transmembrane receptors, ion channels, a specialized membrane-associated periodic skeleton (MPS) rich in F-actin and spectrin, parallel microtubules (MT) that are bundled and interlinked through tripartite-motif-containing 46 (TRIM46; van Beuningen et al., 2015), as well as dynamic EB3-positive MTs. Those components are coordinated by by the master scaffolding protein Ankyrin-G (AnkG; Leterrier et al., 2015). Throughout the entire cell, MT tracks provide the basis for long-distance transport, including that of recycling organelles. The clearance of damaged cellular components is mediated to a large part by acidic vesicular organelles, such as late endosomes and lysosomes, as well as a range of autophagic vesicles which are present along the axon. Over the past years, disturbances in clearance pathways have been identified as a common denominator in many neurodegenerative diseases (Menzies et al., 2017; Pitcairn et al., 2019; Root et al., 2021; Wang et al., 2018), with axonal damage emerging as a major driver of neurodegeneration. In healthy axons, subpopulations of lysosomes delivered from the cell body ensure the timely clearance of damaged proteins (Farfel-Becker et al., 2019), and participate in signaling and RNA trafficking (Liao et al., 2022; Napolitano et al., 2019). Such MT-based transport into the axon is driven by motor proteins whose activity is regulated by selective MT post-translational modifications (PTMs; Park & Roll-Mecak, 2018). Abundant MT PTMs in neurons are tubulin tyrosination and detyrosination. Tyrosinated MT are generated from *de novo* synthesized α-tubulin, which carries the C-terminal tyrosine residue, or by tyrosine ligation to detyrosinated tubulin by the tubulin-tyrosine ligase (TTL; Ersfeld et al., 1993). MT tyrosination has been identified as a marker for dynamic microtubules (Moutin et al., 2021; Tas et al., 2017). MT-detyrosination, which is largely catalyzed by the tubulin-detyrosinase complex vasohibin1/2-small vasohibin binding protein (VASH-SVBP), occurs predominantly in the axon, where it marks a long-lived and stable MT pool (Aillaud et al., 2017; Moutin et al., 2021). Plus-end directed kinesin motors (Cai et al., 2009;

Dunn et al., 2008; Gumy et al., 2013; Homma et al., 2000; Konishi & Setou, 2009; Peris et al., 2009), as well as minus-end directed dynein motor complexes (McKenney et al., 2016; Nirschl et al., 2016; Peris et al., 2006) are known to be sensitive to the tyrosination/detyrosination (Tyr/deTyr)-state of MTs, suggesting a role of MT tyrosination in the regulation of axonal molecular transport.

Here, we used two previously established knockout (KO) mouse models, TTL-KO and SVBP-KO, to characterize the influence of the microtubule Tyr/deTyr status on the structure of the AIS as well as on the axonal transport of acidic endolysosomal organelles. We found that TTL- and SVBP-KO both resulted in an overall shortening of the AIS, without affecting the F-actin nanostructure of the MPS. Furthermore, axons of both TTL- and SVBP-KO neurons contained a higher fraction of immobile endolysosomes, with the mobile fraction displaying markedly decreased run lengths in the retrograde direction. Thus, although VASH-SVBP and TTL activities are known to have opposite effects on MT dynamics (Sanyal et al., 2023), we found that the loss of either enzyme affects AIS structure and axonal trafficking in a similar way, indicating that the regulation of axonal cargo transport relies on maintaining a fine balance between MT tyrosination and detyrosination.

Results

Alterations of the microtubule Tyr/deTyr status do not affect the AIS F-actin organization

We first quantified the tubulin Tyr/deTyr ratios via immunoblot analysis of tyrosinated, detyrosinated and total α-tubulin in primary wildtype (WT), SVBP-KO and TTL-KO cultured cortical neurons obtained from mouse embryos, whose genotypes were determined via PCR (Fig. S1). As expected, the Tyr/deTyr ratio was increased in SVBP-KO neurons (22.540 ± 3.804) and dramatically reduced in TTL-KO neurons (0.010 ± 0.003; Fig. 1B,C). It was previously shown that neurons of TTL-KO mice exhibit premature axon differentiation and formation of supernumerary axons, suggesting that enrichment of stable, detyrosinated MTs induces axon formation (Erck et al., 2005; Peris et al., 2009). In contrast, SVBP-KO neurons, devoid of VASH-SVBP carboxypeptidases, exhibit a delay in their axon development and reduced axonal length (Aillaud et al., 2017; Pagnamenta et al., 2019). To investigate whether this would also have deleterious effects on the AIS structure, we conducted stimulated emission-depletion (STED) microscopy in primary hippocampal neurons to visualize the F-actin-spectrin MPS (Leterrier et al., 2015). AIS were identified by beta-4-spectrin immunostaining, and the nanostructure of F-actin inside the AIS was visualized using a phalloidin-dye (Fig. 1D, E). We found that neither an

increase (SVBP-KO) nor a reduction (TTL-KO) of the Tyr/deTyr ratio interfered with the formation of the MPS or the presence of F-actin patches in the AIS (Fig. 1E). F-actin and beta-4-spectrin form an intercalated submembrane scaffold complex with a 190 nm periodicity (Vassilopoulos et al., 2019), which was equally present in WT, SVBP-KO and TTL-KO, as judged by an autocorrelation analysis of the longitudinal F-actin signal along the AIS (Fig. 1F). Since the cargo-barrier-function of the AIS relies specifically on F-actin patches present inside the AIS (Song et al., 2009; Watanabe et al., 2012), we compared average patch size and number of patches per 10 µm between the different genotypes, and found that none of those metrics was significantly different from WT in the two KOs (Fig. 1G, H). We therefore consider it unlikely that the F-actin-dependent barrier function of the AIS is negatively impaired in either SVBP- or TTL-KO.

SVBP-KO and TTL-KO both lead to a shortening of the AIS

Apart from the cargo filtering function of the AIS, polarized trafficking is additionally instructed by uniformly oriented axonal MTs, which are bundled tightly by the protein TRIM46 inside the AIS (van Beuningen et al., 2015). We therefore decided to compare the distribution of two AIS markers, AnkG and TRIM46, in proximal axons of KO and WT mouse hippocampal neurons. To determine whether expression levels of either protein were altered in KO neurons, we quantified the AnkG/tubulin (Fig. 2A) and TRIM46/tubulin (Fig. 2B) ratios via immunoblot analysis and found no significant difference between WT and KOs (Fig. 2A, B). Next, to investigate whether formation of the AIS was impaired in SVBP or TTL-KO, we quantified AnkG and TRIM46 signals in immunostainings using a MATLAB script based on previously established criteria (Grubb & Burrone, 2010; Supplementary Fig. S2). Representative images of WT and KO neurons stained for TRIM46 (and AnkG for WT) are presented in Fig. 2G-J. In TTL-KO neurons, both markers indicated significantly shortened AIS (AnkG: 21.4 µm, TRIM46: 17.9 µm) compared to WT (AnkG: 27.5 µm, TRIM46: 24.0 µm; Fig. 2G, I, left). The SVBP-KO showed a similar effect on AnkG (25.4 µm; Fig. 2H, left), and a non-significant trend towards shorter AIS with TRIM46 (22.9 µm; Fig. 2F, left). In line with previous observations (Erck et al., 2005), the absence of TTL resulted in a strong supernumerary axon phenotype – more than 50% of the analyzed neurons had two or more AIS emerging from soma or dendrites, while the SVBP-KO produced no such effect (Fig. 2F, H, J). The formation of supernumerary axons was not a determining factor in the reduction of average AIS length, since it occurred both in cells with only one axon, and cells with supernumerary axons (Fig. 2G, I, middle and right panels).

Lysotracker-positive organelles in the distal axon are proteolytically active

Next, we set out to analyze how shifting the balance in the MT Tyr/deTyr ratio would impact axonal cargo transport. We decided to investigate the trafficking of lysosomes because they play an important role in axonal homeostasis (Farfel-Becker et al., 2020), and lysosomal transport was shown to be affected by the Tyr/deTyr state of MT (Mohan et al., 2019). For this we used two-compartment microfluidic chambers (MFCs; Fig. 3A) and Lysotracker, a pH-sensitive dye that non-discriminately labels acidic organelles, including late endosomes, lysosomes and autophagic vesicles. As there is some debate in the literature regarding bona fide degradation-competent lysosomes being present in distal axonal compartments (Farfel-Becker et al., 2019; Lie et al., 2021), we measured the correlation between Lysotracker fluorescence and fluorescence of Magic Red - a specific substrate of the lysosomal, proteolytically active form of cathepsinB (Ni et al., 2022) which fluoresces upon proteolytic cleavage (Fig. 3C). We found that the fluorescence intensity of Lysotracker correlated strongly with the fluorescence intensity of Magic Red (R^2 = 0.9258; Fig. 3C, D), indicating that most Lysotracker-positive vesicles in the distal axon contained active cathepsinB. However, given that both Magic Red and Lysotracker label a range of acidic endo-lysosomal compartments, it should be noted that a spectrum of degradative organelles will be visualized with these probes. For simplicity, from this point on we will use the term “endolysosomes” to refer to those Lysotracker-positive organelles, which is also found in the wider literature (Keren-Kaplan et al., 2022; Roney et al., 2022; van Bommel et al., 2019).

Microtubule tyrosination status affects axonal retrograde trafficking of endolysosomes

We next investigated whether the Tyr/deTyr status of MTs had a differential impact on endolysosomal organelle transport in the axonal compartment of hippocampal neurons grown in two-compartment MFCs. To minimize investigator bias and inconsistencies of manual analysis, we developed a semi-automated analysis workflow to analyze kymographs from individual axons (Fig. 4A; Fig. S3, https://github.com/HU-Berlin-Optobiology/AIS-project.git). Using this setup, we compared various trafficking parameters between SVBP-KO (Fig. 4B, Movie 1), WT (Fig. 4C, Movie 2), and TTL-KO (Fig. 4D, Movie 3). The investigated parameters included the number of mobile and immobile vesicles, pausing times, net direction of transport, velocity, and run lengths (Fig. 4E-L). In TTL-KO neurons, a significantly higher median number of endolysosomes was detected compared to WT (2.0 and 1.8, respectively; Fig. 3E). We observed a strong increase in the proportion of completely stationary organelles in both SVBP (61%) and TTL-KO (69%)

compared to WT (56%; Fig. 3F). Endolysosomes in SVBP-KO neurons (19.5 sec) took longer pauses than WT (16.4 sec), which was not the case for TTL-KO (16.7 sec; Fig. 3G). In the axon, anterograde transport is carried out by plus-end directed kinesin motors, while retrograde movement is mediated by minus-end directed dynein motors. We analyzed the net displacement in the anterograde vs. retrograde direction and observed that in WT, endolysosomes underwent a net retrograde displacement (median -9.1 µm). This was also true for TTL-KO (median -5.9 µm), but interestingly not for SVBP-KO, which showed a net anterograde displacement (median +3.9 µm; Fig. 3H). Anterograde transport, including median velocity (WT 0.43 µm/sec; Fig. 3I) and run distances (WT 5.88 µm; Fig. 3J), was unaffected by lack of either TTL or SVBP. Retrograde transport showed reduced median velocities in SVBP-KO (0.43 µm/sec) compared to WT (0.48 µm/sec; Fig. 3K), and significantly shorter median run lengths in both genotypes (SVBP-KO 6.11 µm; TTL-KO 6.14 µm, WT 8.71 µm; Fig. 3L). Taken together, our findings indicate that retrograde trafficking of endolysosomes is influenced by the tyrosination/detyrosination state of microtubules.

shRNA knockdown of TTL leads to an increase in stationary Lysotracker-positive vesicles

Since defects in early neuronal polarization observed in TTL-KO neurons (Fig. 2F, H, J) could potentially impact axonal trafficking at later stages, we wanted to test whether an increase in the relative amount of deTyr-MT after the establishment of neuron polarity would lead to a similar trafficking phenotype. We therefore conducted trafficking experiments where we knocked down the TTL enzyme after DIV5 in WT mouse hippocampal neurons, i.e. after axon and dendrite specification (Dotti et al., 1988). Expression of the shRNA knockdown construct reduced TTL levels in DIV12/13 neurons by 20% (Fig. S4A) and led to a significant decrease of the Tyr/deTyr tubulin ratio (to 85% of control) in transfected cells (Fig. S4B). Using this approach on neurons grown in MFCs, we conducted the same Lysotracker-trafficking experiments as described above, summarized in Fig. 5. Most of the investigated parameters were similarly unaffected by TTL knockdown as by TTL-KO, such as pause duration (Fig. 5C), net displacement (Fig. 5D), anterograde and retrograde velocities (Fig. 5E, G) and anterograde run distance (Fig. 5F). Contrary to TTL-KO, TTL shRNA knockdown did not affect the average numbers of Lysotracker-labelled vesicles (Fig. 5A) or retrograde run distances (Fig. 5H). However, following TTL shRNA knockdown, the relative amounts of stationary vesicles were significantly increased (median 46%, control 40%; Fig. 5B), similar to TTL-KO (median 69% vs 56% in WT; Fig. 3F). This indicates that even a moderate tip in the Tyr/deTyr MT balance caused by TTL knockdown perturbed the efficient trafficking of axonal endolysosomes.

Discussion

In this study, we aimed to investigate whether MT tyrosination and detyrosination play an instructive role in polarized axonal transport, specifically focusing on the AIS structure and long-range secretory organelle trafficking. We compared neurons from two knock-out mouse lines – one lacking tubulin tyrosine ligase, leading to a strong increase in the Tyr/deTyr ratio, and the other lacking SVBP, resulting in a substantial decrease of the Tyr/deTyr ratio. Confocal and STED imaging revealed that both knockouts resulted in a shortened AIS, without affecting the F-actin organization. Subsequently, using microfluidic devices, we compared axonal trafficking in the different genotypes, using acidic endolysosomes as a representative example of highly motile organelles abundant in the axon and crucial for axonal function. Despite opposite effects on microtubule dynamics, manipulating the balance of MT tyrosination/detyrosination in either direction resulted in surprisingly similar defects in axonal organelle transport. A less drastic reduction in TTL expression through shRNA knockdown partially recapitulated the TTL-KO phenotype, leading to an increase of completely immobile organelles. This suggests that even a moderate shift in the Tyr/deTyr MT ratio affects the trafficking of axonal endolysosomes.

Previous studies using TTL-KO and SVBP-KO mice have mostly focused on morphological and behavioral phenotypes. Notably, the KO of TTL causes perinatal death, which is in part due to a disorganization of neuronal networks. While general organogenesis was normal in these mice, they showed breathing defects and ataxia, likely caused by perturbed neocortical layering and cortico-thalamic loop formation (Erck et al., 2005). Conditional TTL-KO in the forebrain led to viable and fertile mice that had deficits in spatial learning and increased anxiety. These mice showed several CNS defects such as incomplete development of the corpus callosum and the anterior commissures, and in the hippocampus a reduced number of dendritic spines and impaired synaptic plasticity (Hosseini et al., 2022). In contrast to TTL-KO, SVBP-KO mice are viable and fertile, but their brain volume is decreased overall by 7% with over 30% reduction in some white matter tracts. They present behavioural defects like mild hyperactivity, lower anxiety and impaired social behaviour, while memory defects have not been reported (Pagnamenta et al., 2019). Until now there has been no study directly addressing the electrophysiological properties of TTL and SVBP-KO neurons in terms of probability of action potential generation. In light of our results showing that both TTL-KO and SVBP-KO neurons have shorter AIS compared to WT, it would be interesting to investigate if this also affects the threshold for action potential generation, or activity-induced homeostatic plasticity of the AIS (Evans et al., 2015).

Super-resolution imaging revealed no changes in the organization of F-actin structures within the AIS. Like the wild type, the AIS of TTL- and SVBP-KO contained the characteristic MPS with a periodicity of about 190 nm. Also, the size and density of F-actin patches were unaltered, which suggests that the cargo filtering function of the AIS is intact in KO neurons (Watanabe et al., 2012). Interestingly however, alterations in the MT Tyr/deTyr state had distinct effects on the AIS marker proteins TRIM46 and AnkG. Immunoblot analysis of KO cultures did not reveal any significant changes in TRIM46 or AnkG proteins levels, although levels varied quite strongly between individual cultures. When quantifying the length distribution of TRIM46 and AnkG along the AIS, we found that the apparent length of the AIS was reduced in both SVBP- and TTL-KO, with loss of TTL having a stronger effect than SVBP. While TRIM46 and AnkG mark distinct sub-domains within the AIS and control different molecular mechanisms, they are both essential for the formation of the AIS during neuronal development and function in interdependent pathways. TRIM46 is a very early marker for neuronal polarization and localizes to the future axon even before axon specification and before AnkG clustering (van Beuningen et al., 2015) through an unknown mechanism. After axon specification, even though there is no known direct link between AnkG and TRIM46, knockdown of AnkG causes redistribution of TRIM46 (Van Beuningen et al., 2015). This indicates that in adult neurons, TRIM46 localization to the AIS depends on AnkG, and factors that perturb AnkG will likely also affect TRIM46. Apart from that, TRIM46 is known to be carried into the AIS by the kinesin-2 motor complex (Ichinose et al., 2019), which is sensitive to the MT Tyr/deTyr state (Gumy et al., 2013), so the observed reduction of TRIM46 recruitment to the AIS could also be mediated by a less efficient transport in the TTL-KO condition. Finally, as a MT binding protein, TRIM46 itself may favor specific MT PTMs or tubulin isotypes that are only present at the proximal axon, even though none of the modifications known to date specifically mark the position of the AIS (Janke & Kneussel, 2010). Factors that delimit the length of the TRIM46-associated bundles inside the AIS, or the extent of the AIS itself, are currently still unknown (Yang et al., 2019), and are interesting targets for future investigations.

To examine the effect of MT Tyr/deTyr on long-distance transport processes in the distal axonal compartment of hippocampal neurons, we opted to use Lysotracker to label acidic organelles, which are abundant and highly motile in this compartment. We observed largely balanced bi-directional transport of Lysotracker-positive organelles, with a slight predominance of retrograde transport in WT and TTL-KO neurons. These results are in contrast to a previous report, which showed that in developing cortical neurons, acidified and lysosomal-associated membrane protein 1 (LAMP1)-positive organelles move almost exclusively in the retrograde direction (Lie et

al., 2021). LAMP1 is a transmembrane protein that localizes to mature lysosomes, but also labels a wide range of other autophagic, endolysosomal and secretory vesicles (Cheng et al., 2018). Using a ratiometric pH indicator, Lie et al. (2021) report that highly acidic LAMP1 vesicles exhibited predominantly retrograde transport, though most were immobile, while weakly acidic LAMP1 vesicles traveled bidirectionally at a wide range of velocities, in both retrograde and anterograde directions (Lie et al., 2021). It is interesting to note this difference to the behavior of Lysotracker-positive vesicles in our study, which likely stems from the different ranges of organelle identities that were observed, but could also be explained by the different neuronal subtypes used in the studies (hippocampus vs cortex), as well as different ages of the cultures and culture conditions.

Intriguingly, in SVBP-KO neurons we observed a change in overall net displacement directionality, from net retrograde displacement to net anterograde displacement. This might be a reflection of the fact that mainly retrograde transport seemed to be affected by changes in the MT Tyr/deTyr state in our model system: Endolysosomes in both SVBP-KO and TTL-KO neurons showed decreased retrograde run distances, and additionally decreased retrograde velocity in SVBP-KO. Due to the uniform polarity of axonal MTs, all retrograde trafficking is mediated by the dynein/dynactin complex (Cason et al., 2021; Gowrishankar et al., 2021). It is known that the dynactin subunit p150Glued and the dynein regulator CLIP-170 preferentially bind to Tyr-MT, which in WT neurons are enriched in the distal tip of the axon, to initiate retrograde transport (McKenney et al., 2016; Nirschl et al., 2016; Peris et al., 2006). Although an *in vitro* study has shown that the subsequent continuation of processive motility is unaffected by the Tyr/deTyr state of the MT track (McKenney et al., 2016), the interaction of p150Glued with the MT lattice promotes processive motility of the dynein-complex over a state of passive diffusion (Feng et al., 2020). Since p150Glued preferentially interacts with Tyr-MT, this could potentially explain the effects we see in TTL-KO. To our knowledge, no studies have quantified the processivity, binding affinity or velocity of dynein/dynactin on tyrosinated vs detyrosinated MT. The mechanistic explanation of why we observed reduced retrograde movement speed and run length in the SVBP-KO is intriguing and remains open at this point, and it is likely to be complicated by an altered environment of microtubule-associated proteins (Monroy et al., 2020), or by a shift in abundancies of other MT PTMs. Of note, a study on lysosome transport on Tyr vs. deTyr MT in non-neuronal epithelial cells has shown that LAMP2-labelled lysosomes are preferentially recruited to deTyr MT by the motor protein kinesin-1, and that they show reduced motility on deTyr MT compared to Tyr MT (Mohan et al., 2019). While axonal LAMP1/Lysotracker-positive lysosomes in hippocampal neurons are also transported by kinesin-1 (Farías et al., 2017), we did not observe any specific effects on anterograde (i.e. kinesin-

mediated) transport in either SVBP-KO or TTL-KO condition. This could be explained by differences in endolysosomal transport regulation between epithelial cells and neurons, and is an interesting point for further investigations in the future.

The fact that changes in the Tyr/deTyr state of MT seemed to predominantly affect retrograde, but not anterograde trafficking is also interesting considering that the maturation of both endolysosomes and autophagosomes is tightly linked with their retrograde transport through the axon (Cason et al., 2021; Lie et al., 2021). It seems likely that perturbances in the retrograde transport process caused by a change in the Tyr/deTyr ratio would also affect organelle maturation. In this regard, future experiments that focus on organelle identity and maturation state along the axon in combination with the MT Tyr/deTyr status would be highly informative. The defects in axonal transport that we observed in this study most likely also contribute to the altered axon development described for TTL- and SVBP-deficient neurons (Pagnamenta et al., 2019; Peris et al., 2009), and hence in the neural tract abnormalities of TTL- and SVBP-KO mice (Erck et al., 2005; Pagnamenta et al., 2019). Finally, it was recently discovered that TTL expression is reduced in cases of both sporadic and familial Alzheimer's disease, and neurons harboring the familial APP-V717I Alzheimer mutation exhibited decreased MT dynamics (Peris et al., 2022), suggesting a potentially altered regulation of MT-based cargo transport in these diseased neurons. In this regard, TTL shRNA knockdown could be useful as a model to discriminate early developmental defects in the knockout from trafficking phenotypes caused by the reduction in MT tyrosination.

Material and Methods

Animals

All experiments involving animals were carried out in accordance with the European Communities Council Directive (2010/63/EU). Experiments using tissue from wildtype C57BL/6J mice were carried out in accordance with the national Ani mal Welfare Act of the Federal Republic of Germany (Tierschutzgesetz der Bundesrepublik Deutschland, TierSchG) approved by the local authorities of the city-state Hamburg (Behörde für Gesundheit und Verbraucherschutz, Fachbereich Veterinärwesen) and the animal care committee of the University Medical Center Hamburg-Eppendorf, as well as of the Office for Health and Social Welfare (Landesamt für Gesundheit und Soziales, LAGeSo, Berlin, Germany) and the control of the animal welfare officers of the Humboldt University Berlin (reference number T HU-05/22). All experiments involving knockout mice were conducted in accordance with the policy of the Grenoble Institut Neurosciences (GIN) and in compliance with the French legislation. Mice homozygous for an inactivated tubulin tyrosine ligase allele (referred to as TTL-KO), and for an inactivated small vasohibin binding protein allele (referred to as SVBP-KO), were obtained as previously described (Erck et al., 2005; Pagnamenta et al., 2019) and maintained in a C57BL/6 genetic background.

Preparation of microfluidic chambers (MFC)

PDMS and curing agent *(*SYLGARD 184 Silicone Elastomer*)* were mixed thoroughly in a 10:1 ratio in a falcon tube, and centrifuged for 5 min at 4000 g to remove air bubbles. The PDMS was then filled into the epoxy molds and placed under vacuum for 30 min, then polymerized for 3 – 4 hours at 60°C. The cured PDMS patterns were carefully removed from the molds, the wells were cut out using a 4 mm biopsy punch, and the shape of the chambers was cut using a scalpel knife. They were then placed pattern-side down on sticky tape to protect from dust, and stored for up to two weeks. To prepare for use, the MFCs were removed from the sticky tape and vortexed in 96% ethanol for 3-5 min, then washed 3 x with MilliQ water and placed under a sterile hood for air drying. For surface activation, the MFCs were placed in a plasma cleaner, pattern-side up, together with 28 mm glass coverslips placed into 35 mm tissue-culture dishes (without lids), and treated with plasma for 30 sec. The chambers were then placed upside down on the glass coverslips as quickly as possible, then the lids were placed on the dishes and the chambers were baked for another 15-30 min at 60°C. For sterilization, the MFC inside the culture dishes

were placed in a sterile hood under UV light for 20 min. They were then placed inside a 15 cm petri dish together with a piece of sterilized Whatman filter paper wetted with MilliQ water to prevent drying out of the chambers. For neuronal culture, the chambers were either coated with poly-L-lysine as described below (Lysotracker for kymograph analysis, Fig. 4) or with 0.01 mg/mL Poly-L-ornithine-hydrobromide (Sigma, Cat# P3655) in PBS overnight at room temperature (RT) washed twice with MilliQ water and incubated with 2.8 µg/mL Laminin (Bio-Techne, Cat# 3400-010-02) in PBS for 1 h at 37 °C (Lysotracker and Magic Red analysis, Fig. 3). Then they were washed twice with MilliQ water and stored with Hank's Balanced Salt Solution (HBSS, Sigma, Cat# H9269) at 37 °C.

Coating of Culture Dishes for Hippocampal Neurons

Glass coverslips and microfluidic chambers were coated with 1 mg/ml poly-L-lysine (Sigma #P-2636) in borate buffer (3.1 mg/ml boric acid, 4.75mg/ml borax, pH = 8.50) overnight at room temperature. The dishes were then subjected to a short rinse, a long rinse (1 hour), and 2 short rinses with sterile water. Finally, DMEM culture medium + 10% horse serum was added to the dishes and brought to 37°C. For STED imaging, high-precision coverslips (Marienfeld, 117580) were used.

Preparation of knockout mouse hippocampal cultures

E18.5 mouse embryos were collected in sterile filtered 1x PBS. The brains were dissected, and the hippocampi were individually collected in 1x Hank's Balanced Salt Solution (HBSS, Gibco #14185-045). Using a sterile plastic pipette, the 2 hippocampi of one embryo were taken in 2 ml of 1x HBSS. Subsequently, 200 µl of 10x trypsin (Gibco #14185-045) was added, gently agitated and incubated at 37 °C for 15 minutes without mixing during incubation. After incubation, the hippocampi were rinsed once with 1x HBSS at room temperature. The supernatant was removed, and 500 µl of DMEM (Life Technologies #31966047) + 10% horse serum (Life Technologies #26050088) at RT was added. Mechanical dissociation was performed by pipetting up and down using a P1000 pipette with a 200 µl pipette tip on top of the 1000 µl tip, up to a maximum of 10 times. For immunostainings, 20 µl of the 500 µl cell suspension were plated on glass coverslips in a 24-well plate containing 1 ml of DMEM + 10% Horse serum. For microfluidic chambers, 35 µl of the 500 µl cell suspension were centrifuged at 1000 g for 2 min, 30 µl of the supernatant were removed, and the cells were resuspended in the remaining 5 µl, and injected into the microfluidic chamber. The four wells of the chamber were then filled up with DMEM + 10% Horse serum. After plating, the cultures were incubated at 37°C with 5% CO2 for

2 hours, before the culture medium was replaced with MACS Neuro Medium (Miltenyi Biotec #130-093-570) supplemented with B27 (Life Technologies #17504044).

Preparation of knockout mouse cortical cultures

Cortices from E18.5 mouse embryos were collected and treated as hippocampal neuron cultures. After Trypsin incubation and mechanical dissociation, $1x10^6$ cells were seeded in 0.5 mg/ml poly-L-lysine coated 35mm plastic dishes with DMEM + 10% Horse serum for 2 hours, then replaced to MACS Neuro Medium supplemented with B27.

Genotyping

PCR amplifications were performed on alkaline lysates of toe clips or tail cuts of E18.5 mouse embryos. Briefly, mouse tissue was incubated for 30 min at 95°C in alkaline solution (NaOH 25 mM, EDTA 0.2 mM, pH 12.0). Neutralization was performed by adding Tris 40 mM, pH 5.0. Lysates were then analyzed by PCR with corresponding primers and Econo Taq PLUS Green Mix (Euromedex). Primers pairs for testing TTL mouse strain were 5'GGCGACTCCATGGAGTGGTGG and 5'CCCAACATCACATTCTCCAAATATCAAAG (TTL wildtype, 1032 bp) and 5'GATTCCCACTTTGTGGTTCTAAGTACTG and 5' CCCAACATCACATTCTCCAAATATCAAAG (TTL knockout, 900 bp). The four primers were used in a single reaction (Figure S1A). Primers pairs for testing SVBP mouse strain were 5'GATCCACCTGCCCGGAAA and 5'TTTCTTCCAGCACCCTCTCC (SVBP wildtype, 170 bp) and 5'TTTCTTCCAGCACCCTCTCC and 5'CAAACCATGGATCCACGAAA (SVBP knockout, 167 bp). These latter reactions were done separately (Figure S1B). The following amplification protocols were used : (TTL) 95 °C for 5 min, 35 cycles of [95 °C for 1min / 50 °C for 1 min / 72°C for 1 min], 72°C for 2 min ; (SVBP) 95 °C for 5 min, 33 cycles of [95 °C for 30 sec / 50 °C for 30 sec / 72 °C for 30 sec], 72 °C for 2 min. DNAs were analyzed on 1,2 % and 2 % agarose gels for TTL and SVBP, respectively. Pictures of whole agarose gels are shown in Fig. S6.

Immunoblotting

For quantification of tyrosination and detyrosination levels (Fig. 1), cortical neurons were cultured for 15 days in vitro, lysed in Laemmli buffer and boiled at 96°C for 5 minutes. The total protein contents were equilibrated using stain-free 4%-15% gels (Bio-Rad) and then quickly transferred to Nitrocellulose using a Trans-Blot Turbo Transfer System (Bio-Rad). Immunoblots were developed using specific primary antibodies against detyrosinated α-tubulin (1:8000), tyrosinated α-tubulin (1:5000) and total α-tubulin (1:8000). Specific fluorescent secondary antibodies conjugated to Alexa 488 or Cy5 (Jackson Laboratories) were used and analyzed with a ChemiDoc™MP Imaging System (Bio-Rad) using Image Lab software (stain-free gel and

fluorescence protocol) for quantification. For each lane of the blot, the software measures the integrated intensity of the band corresponding to the antigen of interest. The signal of each modified tubulin (tyrosinated or detyrosinated) was normalized to the signal of total α-tubulin of the same lane and the ratio of normalized signals was calculated. One neuronal culture per embryo was processed as indicated and for each neuronal culture, 3 independent blots were performed. For analysis of AnkG and TRIM46 protein levels (Fig. 2), primary cortical neurons from SVBP-KO, TTL-KO and WT animals were lysed in Laemmli buffer at DIV11 and samples were boiled at 96°C for 5 min. The proteins were separated by 10% SDS-PAGE and transferred to PVDF membranes (BioRad Immun-Blot PVDF, Cat# 1620177). After transfer, the membranes were blocked with 5% milk powder in TBS-T (TBS with 0.1% Tween 20) for 1 h at RT. Then, the membranes were incubated with antibodies against AnkG (EMD Millipore, Cat# MABN466, mouse, 1:500 dilution), TRIM46 (Proteintech, Cat# 30298-1-AP, rabbit, 1:2000 dilution) and α-tubulin (Sigma, Cat# T5168, mouse 1:2000 dilution) diluted in TBS-A (TBS with 0.0005% sodium azide) at 4°C over night. Membranes were washed thrice in TBS-T (each wash at RT for 10 min) and incubated with secondary antibodies anti-mouse HRP (Dianova, Cat# 115-035-146, goat, 1:10 000 dilution) or anti-rabbit HRP (Dianova, Cat# 111-035-144, goat, 1:10 000 dilution) diluted in 5% milk powder in TBS-T at RT for 90 min. Afterwards blots were washed twice with TBS-T and once with TBS (each wash at RT for 10 min) and developed using self-made enhanced chemiluminescence solution (100 mM Tris pH8.8, 1.25 mM luminol, 2 mM 4-iodophenylboronic acid, 4.9 mM H_2O_2) (Haan & Behrmann, 2007). Signals were detected with a BioRad ChemiDoc MP Imaging System and analyzed with Fiji's Analyze gel function. For AnkG all 3 visible bands above 100 kDa were measured and summed up. The ratio of AnkG and TRIM46 integrated intensity to integrated intensity of α-tubulin (detected on the same membrane) was formed and values were normalized to the mean of WT. Uncropped blots are available in the supplementary materials, Spectra HR (Thermo Fisher Scientific, Cat# 26625) was used as a protein ladder. Original western blot images can be found in the supplementary materials, Fig. S5 and S6. Details on antibodies can be found in Supplementary Table 1.

Wildtype mouse culture for TTL shRNA knockdown

P0 "wildtype" C57BL/6J mouse pups were decapitated, the brains were dissected in ice-cold HBSS (Sigma, H9269), and the hippocampi of several animals were collected in 450 µl cold HBSS. 50 µl trypsin (Gibco, 12499-015) were added to a final concentration of 0.025% and incubated for 15 min at 37°C. After 2 x washes with 500 µl warm HBSS, the hippocampi were resuspended in 1 ml warm plating medium (DMEM (Gibco, 41966-029) with 10% FBS and 1%

Penicillin/Streptomycin (Invitrogen, 15140122)) and mechanically dissociated by carefully pipetting up and down through two different needles with different pore sizes (yellow 20G and brown 26G) with a 2 ml syringe, up to 4 times each. The cells were counted manually using a Neubauer chamber by staining 15 µl of the cell suspension with trypan blue. For microfluidic chambers, 70.000-80.000 cells were centrifuged at 1000 g for 2 min, the supernatant was removed, and the cells were resuspended in 5 µl plating medium, and injected into the microfluidic chamber. The four wells of the chamber were then filled up with plating medium, and the cultures were incubated at 37°C with 5% CO2 for 2 hours before the culture medium was replaced with growth medium (Neurobasal A (Thermo Fisher, 12349015) supplemented with 1 x B27 Plus (Thermo Fisher, A3582801), 4 mM Glutamax (Gibco, 35050061) and 1 mM sodium pyruvate (Gibco, 11360070)). The cells were then transduced on DIV5 by the addition of AAV, containing either TTL shRNA or control shRNA expression vectors (Supplementary Table 1), directly into the cell medium. 7-8 days after transduction (DIV12-13; Fig. S4), neurons were imaged with Lysotracker Red as described below.

Dual imaging of Magic Red and Lysotracker Green

Magic Red™ was reconstituted with DMSO, aliquoted and stored at -80 °C according to the manufacturer's instructions. Primary hippocampal neurons were prepped from C57BL/6 P0 mice. 80 000 cells were plated into the somatodendritic compartment of a 2-compartment microfluidic chamber (MFC). At DIV14 the MFC was placed in a stage top incubator (okolab) at 37 °C, 5 % CO2 and 90 % humidity atmosphere at the microscope. LysoTracker™ Green DND-26 (ThermoFisher Scientific, Invitrogen™, L7526) and Magic Red™ (Biomol, Immunochemistry Technologies, ICT-937) were diluted in the conditioned medium to final dilutions of 1:10.000 for LysoTracker™ and 1:250 for Magic Red™ and added back to both the somatodendritic and axonal compartment of the MFC. After short incubation, confocal imaging was performed with a Nikon Eclipse Ti-E Visitron SpinningDisk confocal microscope controlled by VisiView software (Visitron Systems). The samples were imaged using a 100× TIRF objective (Nikon, ApoTIRF 100×/1.49 oil) resulting in a pixel size of 65 nm with 488 and 561 nm excitation laser. Lasers were coupled to a CSU-X1 spinning-disk (Yokogawa) unit via a single-mode fiber. Emission light was collected through a filter wheel with filters for GFP (Chroma ET525/50m) and RFP (ET609/54m). Z-stacks were acquired with a pco.edge 4.2 bi sCMOS camera (Excelitas PCO GmbH) with 350 nm step size in 16-bit depth. For image analysis, the FIJI plugin "ComDet" (v.0.5.5) was used to detect particles in the green channel (Lysotracker-positive organelles). The detected ROIs were then used to measure fluorescence intensity in both the

green and red channels.

Immunocytochemistry

Cells were fixed in 4% Roti-Histofix (Carl Roth), 4% sucrose in PBS for 10 min at RT, and washed three times with PBS, before they were permeabilized in 0.2% Triton X-100 in PBS for 10 min. The cells were then washed 3× in PBS and blocked for 45 min at RT with blocking buffer (BB/ 10% horse serum, 0.1% Triton X-100 in PBS). Incubation with primary antibodies was performed in BB at 4°C overnight. After 3× washing in PBS, cells were incubated with corresponding secondary antibodies (see Supplementary Table 1) in BB for 1 h at RT and washed again 3× 10 min in PBS. For STED imaging, the coverslips were subjected to a second overnight incubation step with 1:100 phalloidin-Atto647N (Sigma, 65906) in PBS and washed again 3× 10 min in PBS. As a final step, coverslips were post-fixed in 2% Roti-Histofix, 2% sucrose in PBS for 10 min at RT, washed 3× 10 min with PBS, and mounted on microscope slides using Mowiol. Mowiol was prepared according to the manufacturer's instructions (9.6 g mowiol 4–88 (Carl-Roth, 0713.1), 24.0 g glycerine, 24 ml H_2O, 48 ml 0.2 M Tris pH 8.5, 2.5 g DABCO (Sigma-Aldrich, D27802)). Details on antibodies and other reagents can be found in Supplementary Table 1.

STED Imaging and Analysis

Samples were imaged using an inverted microscope (Axio observer Z1 Zeiss) with a 100x/1.46 objective. The AIS in stained cells was identified by an accumulation of the marker beta-4-spectrin, and the ROI for STED imaging was selected accordingly. STED was performed using the STEDYCON module driven by Imspector software (Abberior Instruments). To achieve STED super-resolution (30 nm pixel size) of STAR Orange and Alexa594, the 561 nm laser was used at 20-30% laser power with the 775 nm depletion laser at 79.95%, and for phalloidin-Atto-647N, the 640 nm laser was used at 5-10% laser power with the 775 nm depletion laser at 46.5%. The number and size of F-actin patches in the phalloidin-Atto647N STED images were quantified using a self-made Python script in FIJI based on the particle detection plugin as described in Han et al. 2024 (Han et al., 2023; "synpo_det_1.0" https://github.com/HU-Berlin-Optobiology/AIS-project/blob/main/Synpo_det_1.0.py.) Briefly, to remove background structures from phalloidin images, the AIS was manually outlined in FIJI using the polygon selection tool, and the ROIs were fed into the "synpo_det" script with the following detection parameters: intensity threshold ("pa_thre") = 0.6, size threshold ("area_thre") = 0.7. The periodicity of the

submembrane F-actin cytoskeleton was analyzed as described in (Vassilopoulos et al., 2019), using the code available on GitHub (https://github.com/cleterrier/Process_Profiles/blob/master/Autocorrelation_.js). ROIs for the script were manually drawn over a stretch of the AIS with visibly good phalloidin staining using the "segmented line" tool in FIJI.

Confocal Imaging of AIS markers

Z-stack images of fixed neurons were acquired on Leica TCS SP8 and Leica TCS SP5 confocal microscopes with 488 nm, 568 nm and 633 nm excitation lasers using a 63.0×1.40 NA oil objective. The pixel size was set to 90 nm and Z-steps varied between 250 and 350 nm.

Live imaging of Lysotracker in knockout and wildtype neurons

Live imaging of knockout cultures grown in MFC was conducted on DIV12. Lysotracker Red DND-99 (ThermoFisher Scientific, L7528) was diluted in the conditioned medium to a final dilution of 1:10 000 and added back to the somatodendritic compartment of the MFC. Lysotracker-stained vesicles became visible in the axonal compartment a few minutes later. Imaging was conducted at 37°C and 5% CO2 on a Zeiss Axio Observer coupled to a spinning disk confocal system (CSU-W1-T3; Yokogawa) connected to an electron-multiplying CCD camera (ProEM+1024, Princeton Instruments). Images were taken every 1 sec for 180 sec with a 63× oil immersion objective (1.46 NA).

Imaging of Lysotracker in TTL knockdown neurons

Live imaging of TTL shRNA knockdown cultures grown in MFC was conducted on DIV12-13. Lysotracker Red DND-99 (ThermoFisher Scientific, L7528) was diluted in the conditioned medium to a final dilution of 1:10 000 and added back to the somatodendritic compartment of the MFC. Lysotracker-stained vesicles became visible in the axonal compartment a few minutes later. shRNA-transfected axons were identified via GFP expression. Imaging was conducted at 37°C and 5% CO2 with a spinning disc confocal microscope (Nikon ECLIPSE Ti) controlled by VisiView software (Visitron Systems) and equipped with the following components: Spinning Disk (Yokogawa), solid-state lasers (488, 561, 647, 405), an EM-CCD camera (Hamamatsu, Digital Camera C9100), and with a 100□×□objective (NA 1.45). The image acquisition rate was 1 fps over 3 min.

Semi-automated analysis of kymographs

Axons of Lysotracker-treated neurons grown in MFC were imaged as above. Timelapse image stacks were processed using FIJI/ImageJ. For shRNA-transfected neurons, individual axons were identified by their GFP expression. For knockout neurons, individual axons were identified by a brightfield image taken before live imaging. Only axons where the directionality could be established (i.e. axons directly coming out of the MFC's microgrooves) were chosen. Individual axons were manually traced using the segmented line tool with a 10-pixel width (pixel size = 0.175 µm). Kymographs were then generated from those ROIs using the KymoResliceWide plugin (https://github.com/UU-cellbiology/KymoResliceWide). The kymographs were then used as input for the bidirectional KymoButler deep learning software (Jakobs et al., 2019, https://github.com/elifesciences-publications/KymoButler) run in Wolfram Mathematica with the following settings: detection threshold=0.2, decision threshold=0.5, minimum particle size=30, minimum frame number=20. Automatically detected traces from KymoButler were loaded into a self-made MATLAB program to overlay them with the original kymograph image, and manually corrected when there was a visible error. The researcher conducting the manual correction was blinded to the data's identities. The corrected tracks were then exported as lists of x-y coordinates, and a self-made Python-based program was used to extract various parameters from the data (see Fig. S3; https://github.com/HU-Berlin-Optobiology/AIS-project.git). In short, the program assigned "movement" if the x-coordinate (x-axis = space) changed from one frame to the next (y-axis = time), and assigned "no movement" if the x-coordinate stayed the same from one frame to the next. Cutoff values were then set to identify "runs" as a continuous movement for 5 frames, and "pause" for continuous non-movement for 5 frames (i.e. a "pause" was defined as a period in which a particle defined as mobile, which had at least one processive run during the imaging period, did not move for 5 or more consecutive frames). Anything below those cutoffs was assigned as "oscillating". A track that did not contain any runs was identified as completely stationary. "Runs" were further divided into anterograde runs and retrograde runs. For each individual identified track, the program calculated the duration of runs and pauses, the run distance and run velocity, and exported those values both individually and as averaged values per each track. Only the run distance and velocity of periods where the particles underwent processive runs for at least 5 consecutive frames were taken into account. For each mobile particle, the net displacement in anterograde or retrograde direction was determined. If a particle moved both in the retrograde and anterograde direction during the imaging period, it might end up having no net displacement ("none") despite being mobile. The threshold for net displacement was set to 5 pixels (0.875 µm).

Statistical analysis

All statistical analysis was conducted in GraphPad Prism 8.02, and Prism 10.2.0. Prism scatter plot appearance was set to “Standard” (Width of distribution of points proportionate to the number of points at that Y value). Error bars show the median ± 95% confidence interval, unless specified otherwise. Data was tested for Gaussian distribution using the D’Agostino & Pearson normality test and accordingly subjected to parametric or non-parametric statistical tests. Statistical analysis of differences between two groups was performed using Student’s t-tests for populations with Gaussian distribution, or Mann-Whitney’s test for non-Gaussian distributions. When comparing 3 or more univariate samples we used one-way ANOVA, or the non-parametric Kruskal-Wallis test. Post-hoc comparisons following Kruskal-Wallis test were done with the non-parametric Dunn test.

Supplementary Information:

Figure S1. Details on genotyping

Figure S2. Details on AIS length calculation

Figure S3. Details on kymograph analysis

Figure S4. Details on TTL shRNA knockdown

Figure S5 (Blot transparency). Western blot source file for Fig. 1

Figure S6 (Blot transparency). Western blot source file for Fig. S1 and Fig. 2

Movie 1. SVBP-KO lysotracker in axon compartment

Movie 2. WT lysotracker in axon compartment

Movie 3. TTL-KO lysotracker in axon compartment

Table S1. Lists crucial reagents and resources (antibodies, other reagents, AAVs)

Acknowledgements

We would like to thank Eitan Zahavi (Weizman Institute of Science, Rehovot) for providing molds for microfluidic devices, Alexander Biermeier (AG Optobiology, HU, Berlin) for help with their production and prepping of primary neurons, Julia Bär for help with prepping primary neurons, Matthias Kneussel (ZMNH, Hamburg) for access to the spinning disc confocal system, Frederic Saudou and Anca Radu (GIN, Grenoble) for help with making MFCs and for access to equipment, Isabelle Jacquier (GIN, Grenoble) for technical help in the preparation of primary neuronal cultures and genotyping, Christophe Bosc (GIN, Grenoble) for help with preparing Fig. S1, Yasmina Saoudi from PIC-GIN, Grenoble, for helping us with confocal and STED microscopy, and Virgilio Failla (UMIF, UKE, Hamburg) for access to the laser scanning confocal microscope. This work was supported by the Photonic Imaging Center of Grenoble Institute Neuroscience (PIC-GIN, Univ Grenoble Alpes – Inserm U1216) which is part of the ISdV core facility and certified by the IBiSA label.

Competing Interests

The authors declare no competing interests.

Funding

This work was supported by Deutsche Forschungsgemeinschaft (Excellence Strategy – EXC-2049–390688087, FOR5228 RP4 and CRC1315 Project A10) to MM, Agence National de la Recherche (ANR), grant SPEED-Y n° ANR-20-CE16-0021 and the Leducq Foundation, research grant n° 20CVD01 to MJM and NeuroCAP-Servier grants to MJM; France Alzheimer (SynapCyAlz AAP PFA 2022) to LP; and the EMBO Scientific Exchange Grant and the JSPS Postdoctoral Fellowship 2023 (Short-term) to AK.

Data availability

N/A

References

Aillaud, C., Bosc, C., Peris, L., Bosson, A., Heemeryck, P., Van Dijk, J., Le Friec, J., Boulan, B., Vossier, F., Sanman, L. E., et al. (2017). Vasohibins/SVBP are tubulin carboxypeptidases (TCPs) that regulate neuron differentiation. *Science*, *358*(6369), 1448–1453. https://doi.org/10.1126/science.aao4165

Cai, D., McEwen, D. P., Martens, J. R., Meyhofer, E., & Verhey, K. J. (2009). Single molecule imaging reveals differences in microtubule track selection between kinesin motors. *PLoS Biology*, *7*(10). https://doi.org/10.1371/journal.pbio.1000216

Cason, S. E., Carman, P. J., Van Duyne, C., Goldsmith, J., Dominguez, R., & Holzbaur, E. L. F. (2021). Sequential dynein effectors regulate axonal autophagosome motility in a maturation-dependent pathway. *Journal of Cell Biology*, *220*(7). https://doi.org/10.1083/jcb.202010179

Cheng, X. T., Xie, Y. X., Zhou, B., Huang, N., Farfel-Becker, T., & Sheng, Z. H. (2018). Revisiting LAMP1 as a marker for degradative autophagy-lysosomal organelles in the nervous system. *Autophagy*, *14*(8), 1472–1474. https://doi.org/10.1080/15548627.2018.1482147

Dotti, C. G., Sullivan, C. A., & Banker, G. A. (1988). The establishment of polarity by hippocampal neurons in culture. *Journal of Neuroscience*, *8*(4). https://doi.org/10.1523/jneurosci.08-04-01454.1988

Dunn, S., Morisson, E. E., Liverpool, T. B., Molina-París, C., Cross, R. A., Alonso, M. C., & Peckham, M. (2008). Differential trafficking of Kif5c on tyrosinated and detyrosinated microtubules in live cells. *Journal of Cell Science*, *121*(7), 1085–1095. https://doi.org/10.1242/jcs.026492

Erck, C., Peris, L., Andrieux, A., Meissirel, C., Gruber, A. D., Vernet, M., Schweitzer, A., Saoudi, Y., Pointu, H., Bosc, C., et al. (2005). A vital role of tubulin-tyrosine-ligase for neuronal organization. *Proceedings of the National Academy of Sciences of the United States of America*, *102*(22), 7853–7858. https://doi.org/10.1073/pnas.0409626102

Ersfeld, K., Wehland, J., Plessmann, U., Dodemont, H., Gerke, V., & Weber, K. (1993). Characterization of the tubulin-tyrosine ligase. *Journal of Cell Biology*, *120*(3), 725–732. https://doi.org/10.1083/jcb.120.3.725

Evans, M. D., Dumitrescu, A. S., Kruijssen, D. L. H., Taylor, S. E., & Grubb, M. S. (2015). Rapid Modulation of Axon Initial Segment Length Influences Repetitive Spike Firing. *Cell Reports*, *13*(6), 1233–1245. https://doi.org/10.1016/j.celrep.2015.09.066

Farfel-Becker, T., Roney, J. C., Cheng, X. T., Li, S., Cuddy, S. R., & Sheng, Z. H. (2019). Neuronal Soma-Derived Degradative Lysosomes Are Continuously Delivered to Distal Axons to Maintain Local Degradation Capacity. *Cell Reports*, *28*(1), 51-64.e4. https://doi.org/10.1016/j.celrep.2019.06.013

Farfel-Becker, T., Roney, J. C., Cheng, X. T., Li, S., Cuddy, S. R., & Sheng, Z. H. (2020). The secret life of degradative lysosomes in axons: delivery from the soma, enzymatic activity, and local autophagic clearance. *Autophagy*, *16*(1), 167–168. https://doi.org/10.1080/15548627.2019.1669869

Farías, G. G., Guardia, C. M., De Pace, R., Britt, D. J., & Bonifacino, J. S. (2017). BORC/kinesin-1 ensemble drives polarized transport of lysosomes into the axon. *Proceedings of the National Academy of Sciences of the United States of America*, *114*(14), E2955–E2964. https://doi.org/10.1073/pnas.1616363114

Feng, Q., Gicking, A. M., & Hancock, W. O. (2020). Dynactin p150 promotes processive motility of DDB complexes by minimizing diffusional behavior of dynein. *Molecular Biology of the Cell*, *31*(8), 782–792. https://doi.org/10.1091/MBC.E19-09-0495

Gowrishankar, S., Lyons, L., Rafiq, N. M., Ferguson, A. R., Camilli, P. De, & Ferguson, S. M. (2021). Overlapping roles of JIP3 and JIP4 in promoting axonal transport of lysosomes in human iPSC-derived neurons. *Molecular Biology of the Cell*, *32*(11), 1094–1103. https://doi.org/10.1091/mbc.E20-06-0382

Grubb, M. S., & Burrone, J. (2010). Activity-dependent relocation of the axon initial segment fine-tunes neuronal excitability. *Nature*, *465*(7301), 1070–1074. https://doi.org/10.1038/nature09160

Gumy, L. F., Chew, D. J., Tortosa, E., Katrukha, E. A., Kapitein, L. C., Tolkovsky, A. M., Hoogenraad, C. C., & Fawcett, J. W. (2013). The kinesin-2 family member KIF3C regulates microtubule dynamics and is

required for axon growth and regeneration. *Journal of Neuroscience*, *33*(28), 11329–11345. https://doi.org/10.1523/JNEUROSCI.5221-12.2013

Haan, C., & Behrmann, I. (2007). A cost effective non-commercial ECL-solution for Western blot detections yielding strong signals and low background. *Journal of Immunological Methods*, *318*(1–2), 11–19. https://doi.org/10.1016/j.jim.2006.07.027

Han, Y., Thuenauer, R., Grünewald, K., & Mikhaylova, M. (2023). Unveiling the cell biology of hippocampal neurons with dendritic axon origin. *Biorxiv*. https://doi.org/https://doi.org/10.1101/2023.09.14.557747

Homma, K., Saito, J., Ikebe, R., & Ikebe, M. (2000). Ca2+-dependent regulation of the motor activity of myosin V. *Journal of Biological Chemistry*, *275*(44), 34766–34771. https://doi.org/10.1074/jbc.M003132200

Hosseini, S., van Ham, M., Erck, C., Korte, M., & Michaelsen-Preusse, K. (2022). The role of α-tubulin tyrosination in controlling the structure and function of hippocampal neurons. *Frontiers in Molecular Neuroscience*, *15*(October), 1–20. https://doi.org/10.3389/fnmol.2022.931859

Ichinose, S., Ogawa, T., Jiang, X., & Hirokawa, N. (2019). The Spatiotemporal Construction of the Axon Initial Segment via KIF3/KAP3/TRIM46 Transport under MARK2 Signaling. *Cell Reports*, *28*(9), 2413-2426.e7. https://doi.org/10.1016/j.celrep.2019.07.093

Janke, C., & Kneussel, M. (2010). Tubulin post-translational modifications: Encoding functions on the neuronal microtubule cytoskeleton. *Trends in Neurosciences*, *33*(8), 362–372. https://doi.org/10.1016/j.tins.2010.05.001

Kapitein, L. C., & Hoogenraad, C. C. (2011). Which way to go? Cytoskeletal organization and polarized transport in neurons. *Molecular and Cellular Neuroscience*, *46*(1), 9–20. https://doi.org/10.1016/j.mcn.2010.08.015

Keren-Kaplan, T., Sarić, A., Ghosh, S., Williamson, C. D., Jia, R., Li, Y., & Bonifacino, J. S. (2022). RUFY3 and RUFY4 are ARL8 effectors that promote coupling of endolysosomes to dynein-dynactin. *Nature Communications*, *13*(1). https://doi.org/10.1038/s41467-022-28952-y

Konishi, Y., & Setou, M. (2009). Tubulin tyrosination navigates the kinesin-1 motor domain to axons. *Nature Neuroscience*, *12*(5), 559–567. https://doi.org/10.1038/nn.2314

Leterrier, C., Potier, J., Caillol, G., Debarnot, C., Rueda Boroni, F., & Dargent, B. (2015). Nanoscale Architecture of the Axon Initial Segment Reveals an Organized and Robust Scaffold. *Cell Reports*, *13*(12), 2781–2793. https://doi.org/10.1016/j.celrep.2015.11.051

Liao, Y. C., Fernandopulle, M. S., Wang, G., Choi, H., Hao, L., Drerup, C. M., Patel, R., Qamar, S., Nixon-Abell, J., Shen, Y., et al. (2019). RNA Granules Hitchhike on Lysosomes for Long-Distance Transport, Using Annexin A11 as a Molecular Tether. *Cell*, *179*(1), 147-164.e20. https://doi.org/10.1016/j.cell.2019.08.050

Lie, P. P. Y., Yang, D. S., Stavrides, P., Goulbourne, C. N., Zheng, P., Mohan, P. S., Cataldo, A. M., & Nixon, R. A. (2021). Post-Golgi carriers, not lysosomes, confer lysosomal properties to pre-degradative organelles in normal and dystrophic axons. *Cell Reports*, *35*(4). https://doi.org/10.1016/j.celrep.2021.109034

McKenney, R. J., Huynh, W., Vale, R. D., & Sirajuddin, M. (2016). Tyrosination of α-tubulin controls the initiation of processive dynein–dynactin motility. *The EMBO Journal*, *35*(11), 1175–1185. https://doi.org/10.15252/embj.201593071

Menzies, F. M., Fleming, A., Caricasole, A., Bento, C. F., Andrews, S. P., Ashkenazi, A., Füllgrabe, J., Jackson, A., Jimenez Sanchez, M., Karabiyik, C., et al. (2017). Autophagy and Neurodegeneration: Pathogenic Mechanisms and Therapeutic Opportunities. *Neuron*, *93*(5), 1015–1034. https://doi.org/10.1016/j.neuron.2017.01.022

Mohan, N., Sorokina, E. M., Verdeny, I. V., Alvarez, A. S., & Lakadamyali, M. (2019). Detyrosinated microtubules spatially constrain lysosomes facilitating lysosome-autophagosome fusion. *Journal of Cell Biology*, *218*(2), 632–643. https://doi.org/10.1083/jcb.201807124

Monroy, B. Y., Tan, T. C., Oclaman, J. M., Han, J. S., Simó, S., Niwa, S., Nowakowski, D. W., McKenney, R. J., & Ori-McKenney, K. M. (2020). A Combinatorial MAP Code Dictates Polarized Microtubule Transport. *Developmental Cell*, *53*(1), 60-72.e4. https://doi.org/10.1016/j.devcel.2020.01.029

Moutin, M. J., Bosc, C., Peris, L., & Andrieux, A. (2021). Tubulin post-translational modifications control neuronal development and functions. *Developmental Neurobiology*, *81*(3), 253–272. https://doi.org/10.1002/dneu.22774

Nakada, C., Ritchie, K., Oba, Y., Nakamura, M., Hotta, Y., Iino, R., Kasai, R. S., Yamaguchi, K., Fujiwara, T., & Kusumi, A. (2003). Accumulation of anchored proteins forms membrane diffusion barriers during neuronal polarization. *Nature Cell Biology*, *5*(7), 626–633.

Napolitano, G., Di Malta, C., & Ballabio, A. (2022). Non-canonical mTORC1 signaling at the lysosome. *Trends in Cell Biology*, *32*(11), 920–931. https://doi.org/10.1016/j.tcb.2022.04.012

Ni, J., Lan, F., Xu, Y., Nakanishi, H., & Li, X. (2022). Extralysosomal cathepsin B in central nervous system: Mechanisms and therapeutic implications. *Brain Pathology*, *32*(5). https://doi.org/10.1111/bpa.13071

Nirschl, J. J., Magiera, M. M., Lazarus, J. E., Janke, C., & Holzbaur, E. L. F. (2016). α-Tubulin Tyrosination and CLIP-170 Phosphorylation Regulate the Initiation of Dynein-Driven Transport in Neurons. *Cell Reports*, *14*(11), 2637–2652. https://doi.org/10.1016/j.celrep.2016.02.046

Pagnamenta, A. T., Heemeryck, P., Martin, H. C., Bosc, C., Peris, L., Uszynski, I., Gory-Fauré, S., Couly, S., Deshpande, C., Siddiqui, A., et al. (2019). Defective tubulin detyrosination causes structural brain abnormalities with cognitive deficiency in humans and mice. *Human Molecular Genetics*, *28*(20), 3391–3405. https://doi.org/10.1093/hmg/ddz186

Park, J. H., & Roll-Mecak, A. (2018). The tubulin code in neuronal polarity. *Current Opinion in Neurobiology*, *51*, 95–102. https://doi.org/10.1016/j.conb.2018.03.001

Peris, L., Parato, J., Qu, X., Soleilhac, J. M., Lante, F., Kumar, A., Pero, M. E., Martínez-Hernández, J., Corrao, C., Falivelli, G., et al. (2022). Tubulin tyrosination regulates synaptic function and is disrupted in Alzheimer's disease. *Brain*, *145*(7), 2486–2506. https://doi.org/10.1093/brain/awab436

Peris, L., Thery, M., Fauré, J., Saoudi, Y., Lafanechère, L., Chilton, J. K., Gordon-Weeks, P., Galjart, N., Bornens, M., Wordeman, L., et al. (2006). Tubulin tyrosination is a major factor affecting the recruitment of CAP-Gly proteins at microtubule plus ends. *Journal of Cell Biology*, *174*(6), 839–849. https://doi.org/10.1083/jcb.200512058

Peris, L., Wagenbach, M., Lafanechère, L., Brocard, J., Moore, A. T., Kozielski, F., Job, D., Wordeman, L., & Andrieux, A. (2009). Motor-dependent microtubule disassembly driven by tubulin tyrosination. *Journal of Cell Biology*, *185*(7), 1159–1166. https://doi.org/10.1083/jcb.200902142

Petersen, J. D., Kaech, S., & Banker, G. (2014). Selective Microtubule-Based Transport of Dendritic Membrane Proteins Arises in Concert with Axon Specification. *Journal of Neuroscience*, *34*(12), 4135–4147. https://doi.org/10.1523/JNEUROSCI.3779-13.2014

Pitcairn, C., Wani, W. Y., & Mazzulli, J. R. (2019). Dysregulation of the autophagic-lysosomal pathway in Gaucher and Parkinson's disease. *Neurobiology of Disease*, *122*(March 2018), 72–82. https://doi.org/10.1016/j.nbd.2018.03.008

Roney, J. C., Cheng, X. T., & Sheng, Z. H. (2022). Neuronal endolysosomal transport and lysosomal functionality in maintaining axonostasis. *Journal of Cell Biology*, *221*(3), 1–16. https://doi.org/10.1083/jcb.202111077

Root, J., Merino, P., Nuckols, A., Johnson, M., & Kukar, T. (2021). Lysosome dysfunction as a cause of neurodegenerative diseases: Lessons from frontotemporal dementia and amyotrophic lateral sclerosis. *Neurobiology of Disease*, *154*, 105360. https://doi.org/10.1016/j.nbd.2021.105360

Sanyal, C., Pietsch, N., Ramirez Rios, S., Peris, L., Carrier, L., & Moutin, M. J. (2023). The detyrosination/re-tyrosination cycle of tubulin and its role and dysfunction in neurons and cardiomyocytes. *Seminars in Cell and Developmental Biology*, *137*(June 2021), 46–62.

https://doi.org/10.1016/j.semcdb.2021.12.006
Song, A. hong, Wang, D., Chen, G., Li, Y., Luo, J., Duan, S., & Poo, M. ming. (2009). A Selective Filter for Cytoplasmic Transport at the Axon Initial Segment. *Cell*, *136*(6), 1148–1160. https://doi.org/10.1016/j.cell.2009.01.016
Tas, R. P., Chazeau, A., Cloin, B. M. C., Lambers, M. L. A., Hoogenraad, C. C., & Kapitein, L. C. (2017). Differentiation between Oppositely Oriented Microtubules Controls Polarized Neuronal Transport. *Neuron*, *96*(6), 1264-1271.e5. https://doi.org/10.1016/j.neuron.2017.11.018
Van Beuningen, S. F. B., Will, L., Harterink, M., Chazeau, A., Van Battum, E. Y., Frias, C. P., Franker, M. A. M., Katrukha, E. A., Stucchi, R., Vocking, K., et al. (2015a). TRIM46 Controls Neuronal Polarity and Axon Specification by Driving the Formation of Parallel Microtubule Arrays. *Neuron*, *88*(6), 1208–1226. https://doi.org/10.1016/j.neuron.2015.11.012
Van Beuningen, S. F. B., Will, L., Harterink, M., Chazeau, A., Van Battum, E. Y., Frias, C. P., Franker, M. A. M., Katrukha, E. A., Stucchi, R., Vocking, K., et al. (2015b). TRIM46 Controls Neuronal Polarity and Axon Specification by Driving the Formation of Parallel Microtubule Arrays. *Neuron*, *88*(6), 1208–1226. https://doi.org/10.1016/j.neuron.2015.11.012
van Bommel, B., Konietzny, A., Kobler, O., Bär, J., & Mikhaylova, M. (2019). F-actin patches associated with glutamatergic synapses control positioning of dendritic lysosomes. *The EMBO Journal*, *38*(15), 1–17. https://doi.org/10.15252/embj.2018101183
Vassilopoulos, S., Gibaud, S., Jimenez, A., Caillol, G., & Leterrier, C. (2019). Ultrastructure of the axonal periodic scaffold reveals a braid-like organization of actin rings. *Nature Communications*, *10*(1), 1–13. https://doi.org/10.1038/s41467-019-13835-6
Wang, C., Telpoukhovskaia, M. A., Bahr, B. A., Chen, X., & Gan, L. (2018). Endo-lysosomal dysfunction: a converging mechanism in neurodegenerative diseases. *Current Opinion in Neurobiology*, *48*(Figure 1), 52–58. https://doi.org/10.1016/j.conb.2017.09.005
Watanabe, K., Al-Bassam, S., Miyazaki, Y., Wandless, T. J., Webster, P., & Arnold, D. B. (2012). Networks of Polarized Actin Filaments in the Axon Initial Segment Provide a Mechanism for Sorting Axonal and Dendritic Proteins. *Cell Reports*, *2*(6), 1546–1553. https://doi.org/10.1016/j.celrep.2012.11.015
Yang, R., Walder-Christensen, K. K., Lalani, S., Yan, H., García-Prieto, I. D., Álvarez, S., Fernández-Jaén, A., Speltz, L., Jiang, Y. H., & Bennett, V. (2019). Neurodevelopmental mutation of giant ankyrin-G disrupts a core mechanism for axon initial segment assembly. *Proceedings of the National Academy of Sciences of the United States of America*, *116*(39), 19717–19726. https://doi.org/10.1073/pnas.1909989116

Figure Legends

Figure 1: Imbalanced MT tyrosination/detyrosination does not affect the nanostructure of the F-actin cytoskeleton in the AIS.

A) Illustration of the tubulin tyrosination/detyrosination cycle. **B, C**) Immunoblot quantifications of the ratio of tyrosinated vs. detyrosinated tubulin from crude lysates of cultured mouse cortical neurons at DIV15 with SVBP-KO (B) and TTL-KO (C) compared to WT neurons. n = 4, 3 independent cultures for WT, SVBP-KO respectively, and 4, 3 independent cultures for WT, TTL-KO respectively. Mann-Whitney test with Dunn's multiple comparison test, ns = non-significant, *p<0.05. **D**) Confocal images of DIV12 neurons stained with phalloidin-647 (F-actin marker) and with an antibody against beta-4-spectrin to identify the AIS. Scale bar = 25 µm. **E)** Representative STED images of F-actin in the AIS of WT, SVBP-KO and TTL-KO neurons. Lower panels show particle detection in FIJI used for quantification of F-actin patches. Scale bar = 2.5 µm. **F)** Average autocorrelation of the F-actin signal periodicity in the different genotypes shows a 190 nm periodicity in WT, SVBP-KO and TTL-KO. Shown is the mean ± SEM. Calculation of autocorrelation was performed as described previously (Vassilopoulos et al. 2019, Material & Methods). **G)** Average size (px²) of F-actin patches present inside the AIS. Medians (with 95% CI) are SVBP-KO 27.65 px² (22.5-44.89), WT 26.22 px² (19.12-33.75), TTL-KO px² 33.8 (24.6-38.33). **H)** Average number of F-actin patches per 10 µm inside the AIS. Medians (with 95% CI) are SVBP-KO 11.1 (6.3-15.1), WT 7.5 (4.2-13.8), and TTL-KO 7.6 (4.1-10.2). (F-H) n = 13, 36, 23 AIS for SVBP-KO (3 independent cultures), WT (6 independent cultures) and TTL-KO (3 independent cultures). (G, H) Mann-Whitney-Test. ns = non-significant.

Figure 2: Both SVBP and TTL-KO lead to shorter AIS in hippocampal neurons.

A) Western blot analysis of AnkG levels in SVBP-KO, TTL-KO and WT DIV11 primary cortical neurons. Right panel: Representative WB against AnkG and total α-tubulin (Tub) as loading control. Left panel: Quantification for the ratios AnkG/Tub normalized to the mean of WT. **B)** Western blot analysis of TRIM46 levels in SVBP-KO, TTL-KO and WT DIV11 primary cortical neurons. Right panel: Representative WB against TRIM46 and total α-tubulin as loading control. Left panel: Quantification for ratios TRIM46/Tub normalized to the mean of WT. (A, B) Individual values and median with 95% CI are shown, n=5 independent cultures, Kruskal-Wallis test with Dunn's multiple comparisons test, ns = non-significant. **C, D)** Example images of WT DIV12 mouse hippocampal neurons stained for the AIS markers TRIM46 (B) or AnkG (C) together with MAP2 (dendritic marker), and DNA (DAPI). Arrows indicate the AIS. **E, F)** Representative images of DIV12 TTL-KO (D) and SVBP-KO (E) neurons stained for MAP2, TRIM46 and DAPI. Arrows indicate AIS. **G, I)** AIS length of TRIM46-stained (G) and AnkG-stained (I) neurons from

SVBP-KO, WT, and TTL-KO mice. Individual values and median with 95% CI are shown. **Left panel:** graphs show all cells analyzed together. **Middle, Right panel:** Graphs show cells with only 1 axon and cells with 2+ axons analyzed separately. **H, J)** Quantification of neurons with supernumerary axons in the different genotypes as judged by TRIM46 (H) and AnkG (J) staining. Error bars indicate mean ± SEM. (G-J): TRIM46: n = 68, 93, 123 AIS for SVBP-KO (2 independent cultures), TTL-KO (5 independent cultures) and WT (6 independent cultures). AnkG: n = 84, 110, 108 AIS for SVBP-KO (3 independent cultures), TTL-KO (4 independent cultures) and WT (5 independent cultures). G, I) Kruskal-Wallis test with Dunn's multiple comparisons test. H,J) Two-way repeated measures ANOVA with Dunnett's multiple comparisons test. ns = non-significant, *p<0.05, **p<0.005, ***p<0.0005, ****p<0.0001.

Figure 3: Lysotracker-positive vesicles in distal axons are degradatively active.

A) Illustration of the 2-compartment MFC used for live-imaging of axonal trafficking (left panel), and microscopy image of DIV12 mouse hippocampal neurons expressing GFP (right panel). **B)** Confocal image of axons inside MFC, labeled with Lysotracker Green and Magic Red. **C)** Integrated density values of Lysotracker correlate with the integrated density of Magic Red. 815 particles were analyzed in three separate locations of one independent neuron culture in an area of approx. 0.2 mm^2. The dotted red line indicates the calculated linear regression (y = 1,578*x + 4,156), Spearman's correlation coefficient r = 0.9258.

Figure 4: The retrograde trafficking efficiency of endolysosomes is similarly decreased in the distal axons of TTL and SVBP-KO hippocampal neurons.

A) Left panel: representative kymograph from individual Lysotracker-treated axons; each trace represents a single organelle. **Right panel:** Kymograph analysis presented on the left using a self-made Python script (for details see Material & Methods). **B-D)** Representative example kymographs for SVBP-KO (B), WT (C) and TTL-KO neurons (D). See also Supplementary Movies 1-3. **E-L)** Summary of vesicle trafficking properties during the imaging period. **E)** Average number of all detected vesicles per 10 µm (mobile and stationary). **F)** Percentage of stationary vesicles. **G)** Average pause duration. **H)** Average net displacement in anterograde or retrograde direction. **I, J)** Average anterograde instant velocities and run distances. **K, L)** Average retrograde instant velocities and run distances. E-L) Individual values and median with 95% CI are shown. n=58, 164, 114 axons from SVBP (3 independent experiments), WT (6 independent experiments) and TTL-KO (5 independent experiments), respectively. Kruskal-Wallis test with Dunn's multiple comparisons test. ns = non-significant, *p<0.05, **p<0.005,

****p<0.0001.

Figure 5: Acute shRNA knockdown of TTL leads to an increase in stationary endolysosomes.

A) Average number of all detected vesicles per 10 µm (mobile and stationary). **B)** Percentage of stationary vesicles. **C)** Average pause duration. **D)** Percent net displacement in anterograde or retrograde direction. **E, F)** Average anterograde instant velocities and run distances. **G, H)** Average retrograde instant velocities and run distances. Individual values and median with 95% CI are shown. n = 90, 57 axons from control (3 independent cultures) and TTL shRNA (3 independent cultures). Mann-Whitney test. ns = non-significant, **p<0.005.

Figure 1

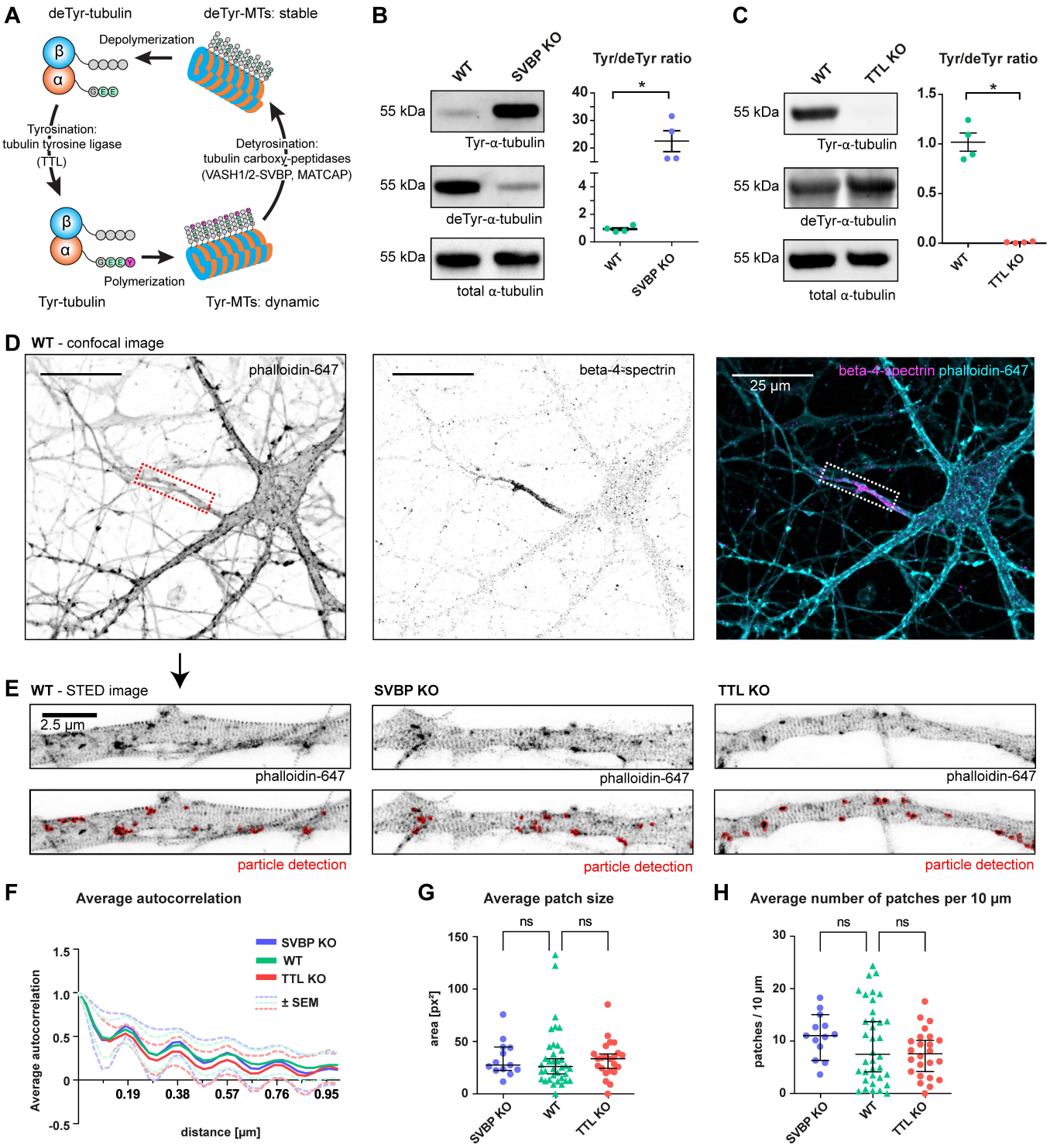
A
deTyr-tubulin
deTyr-MTs: stable
Depolymerization
Tyrosination:
tubulin tyrosine ligase
(TTL)
Detyrosination:
tubulin carboxy-peptidases
(VASH1/2-SVBP, MATCAP)
Polymerization
Tyr-tubulin
Tyr-MTs: dynamic
B
WT
SVBP KO
55 kDa
Tyr-α-tubulin
deTyr-α-tubulin
total α-tubulin
Tyr/deTyr ratio
C
TTL KO
D
WT - confocal image
phalloidin-647
beta-4-spectrin
25 µm
beta-4-spectrin phalloidin-647
E
WT - STED image
SVBP KO
TTL KO
2.5 µm
particle detection
F
Average autocorrelation
SVBP KO
WT
TTL KO
± SEM
Average autocorrelation
distance [µm]
G
Average patch size
ns
area [px²]
H
Average number of patches per 10 µm
patches / 10 µm

Figure 2

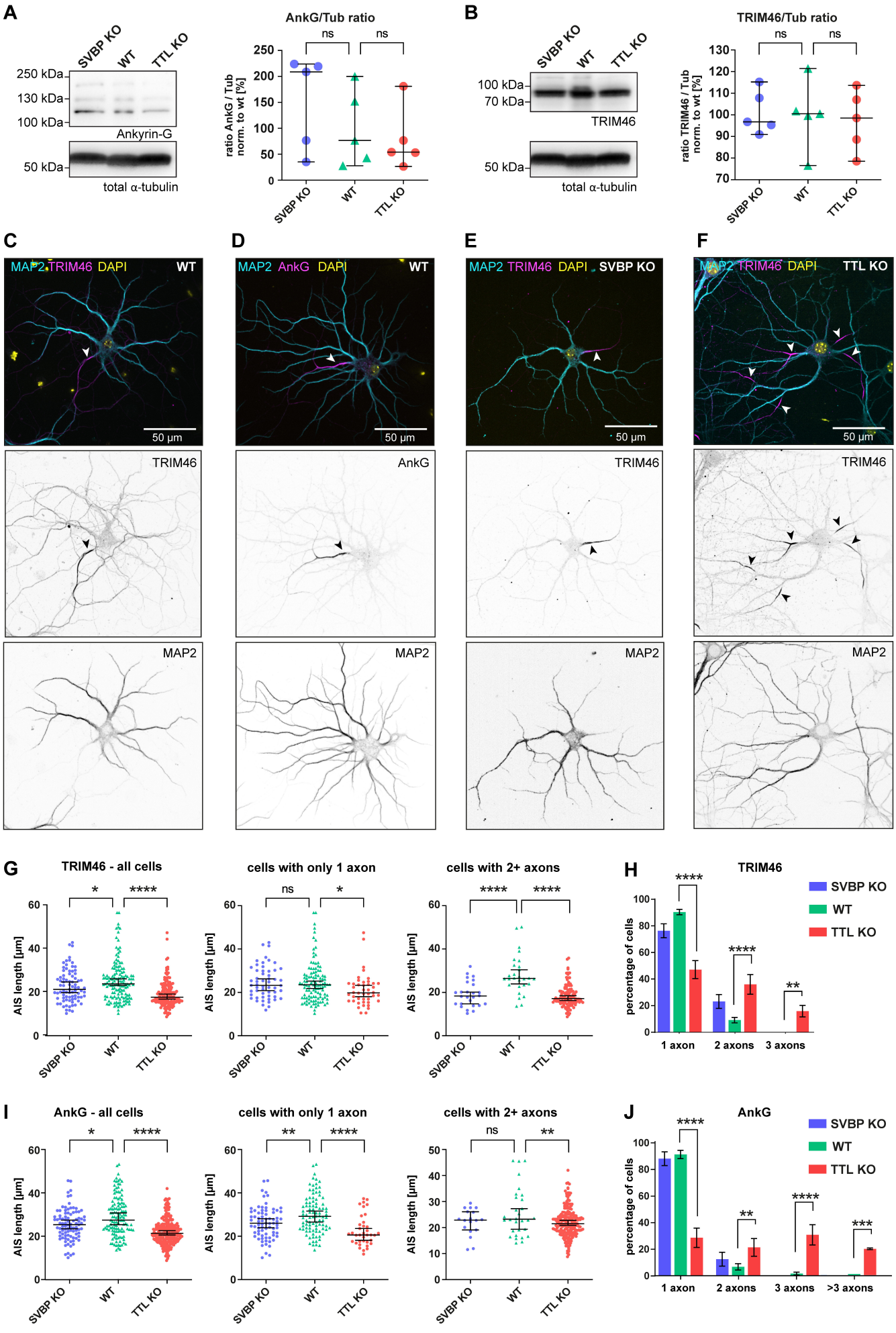
A
SVBP KO
WT
TTL KO
250 kDa
130 kDa
100 kDa
Ankyrin-G
50 kDa
total α-tubulin
AnkG/Tub ratio
ns
ns
ratio AnkG / Tub norm. to wt [%]
B
100 kDa
70 kDa
TRIM46
50 kDa
total α-tubulin
TRIM46/Tub ratio
ratio TRIM46 / Tub norm. to wt [%]
C
MAP2 TRIM46 DAPI
WT
50 µm
TRIM46
MAP2
D
MAP2 AnkG DAPI
WT
AnkG
E
MAP2 TRIM46 DAPI
SVBP KO
F
MAP2 TRIM46 DAPI
TTL KO
G
TRIM46 - all cells
cells with only 1 axon
cells with 2+ axons
AIS length [µm]
H
TRIM46
percentage of cells
1 axon
2 axons
3 axons
I
AnkG - all cells
cells with only 1 axon
cells with 2+ axons
AIS length [µm]
J
AnkG
percentage of cells
1 axon
2 axons
3 axons
>3 axons

Figure 3

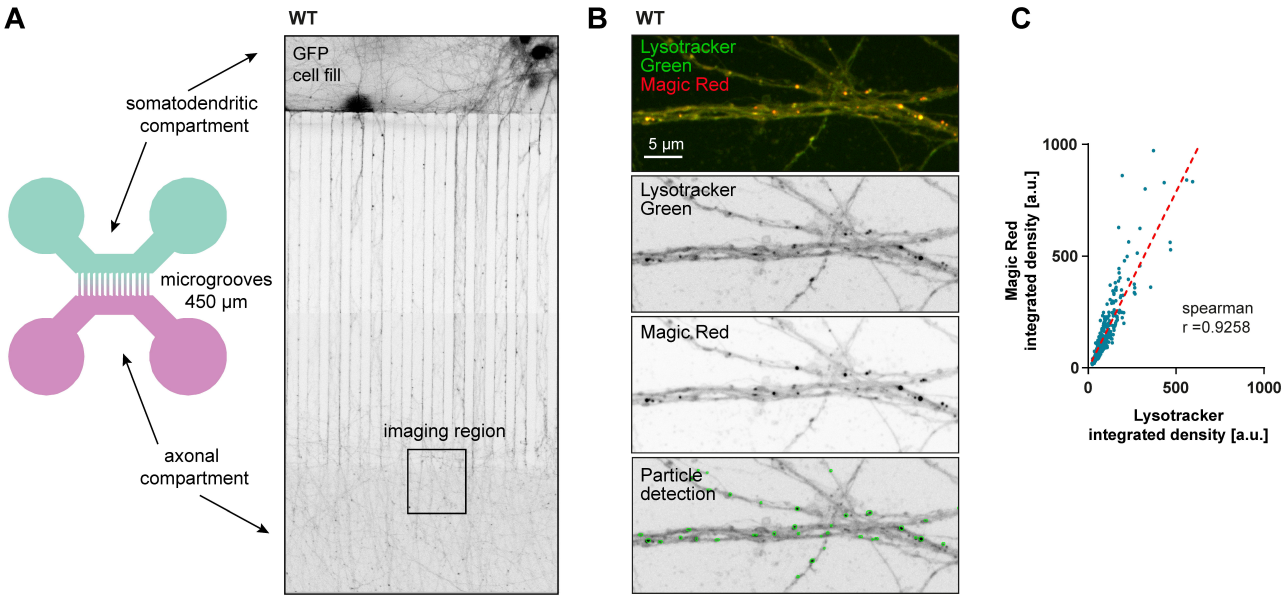
A
WT
somatodendritic compartment
microgrooves 450 µm
axonal compartment
GFP cell fill
imaging region
B
WT
Lysotracker Green Magic Red
5 µm
Lysotracker Green
Magic Red
Particle detection
C
Magic Red integrated density [a.u.]
Lysotracker integrated density [a.u.]
spearman r =0.9258
0
500
1000

Figure 4

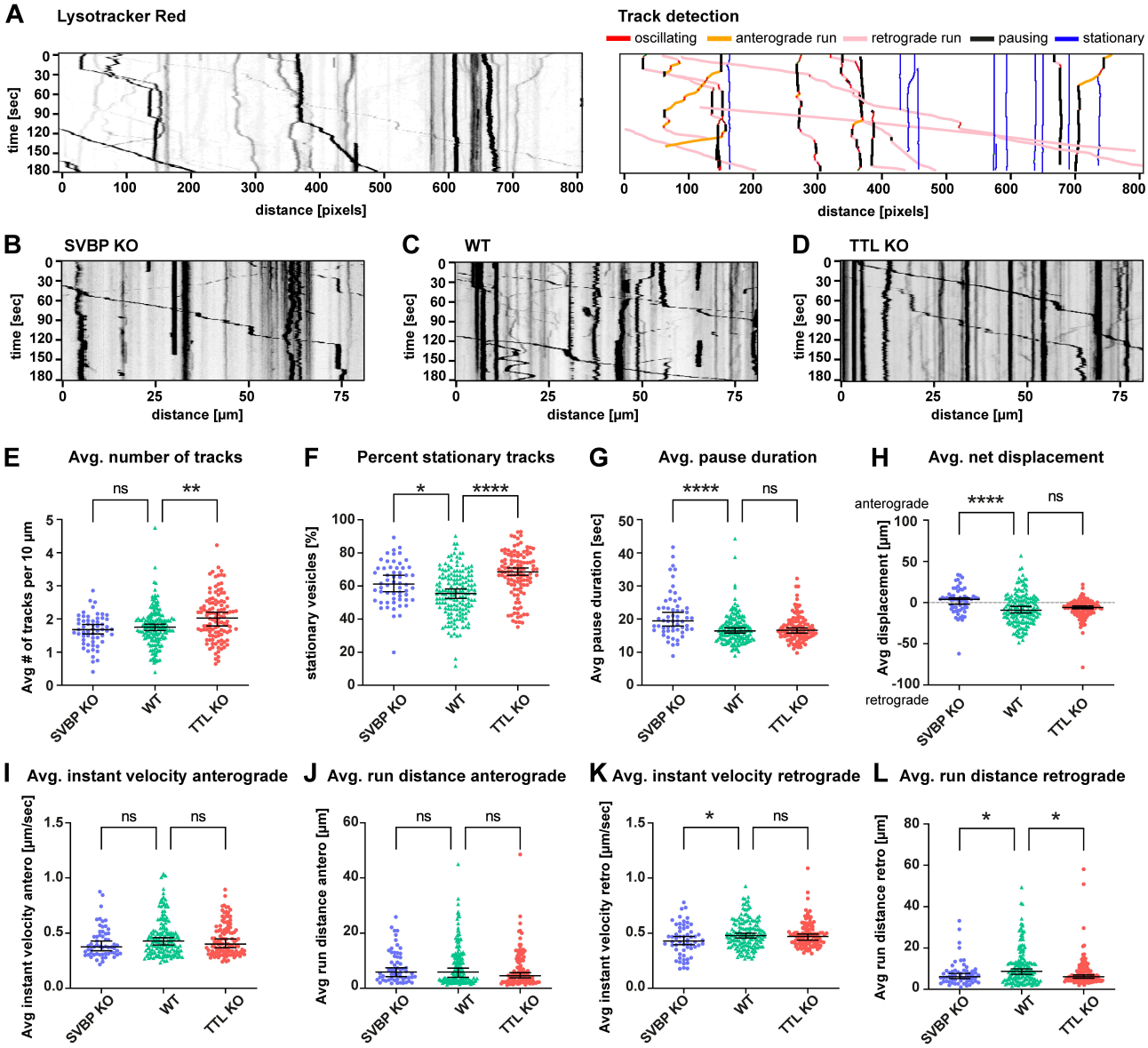
A
Lysotracker Red
time [sec]
distance [pixels]
Track detection
oscillating
anterograde run
retrograde run
pausing
stationary
distance [pixels]
B
SVBP KO
C
WT
D
TTL KO
distance [µm]
E
Avg. number of tracks
Avg # of tracks per 10 µm
F
Percent stationary tracks
stationary vesicles [%]
G
Avg. pause duration
Avg pause duration [sec]
H
Avg. net displacement
anterograde
retrograde
Avg displacement [µm]
I
Avg. instant velocity anterograde
Avg instant velocity antero [µm/sec]
J
Avg. run distance anterograde
Avg run distance antero [µm]
K
Avg. instant velocity retrograde
Avg instant velocity retro [µm/sec]
L
Avg. run distance retrograde
Avg run distance retro [µm]
SVBP KO
WT
TTL KO
ns
*
**
****

Figure 5

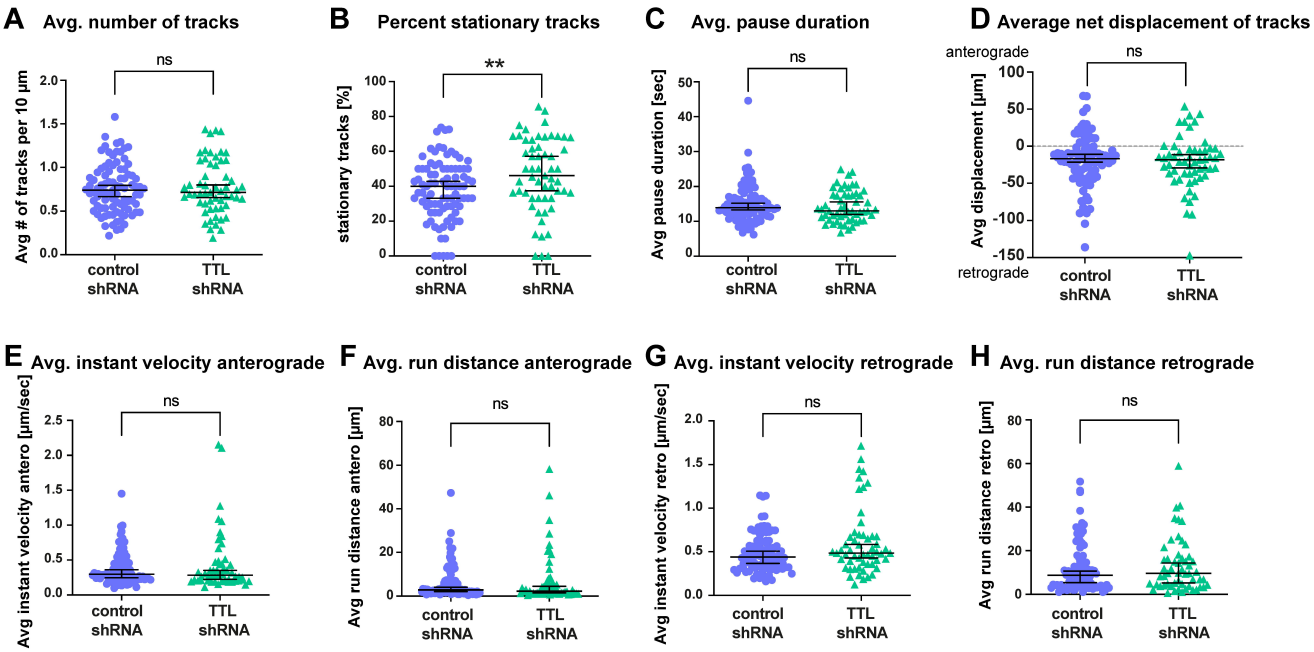
A
Avg. number of tracks
Avg # of tracks per 10 µm
ns
control shRNA
TTL shRNA
B
Percent stationary tracks
stationary tracks [%]
**
C
Avg. pause duration
Avg pause duration [sec]
D
Average net displacement of tracks
anterograde
retrograde
Avg displacement [µm]
E
Avg. instant velocity anterograde
Avg instant velocity antero [µm/sec]
F
Avg. run distance anterograde
Avg run distance antero [µm]
G
Avg. instant velocity retrograde
Avg instant velocity retro [µm/sec]
H
Avg. run distance retrograde
Avg run distance retro [µm]